The Effects of Bistatic Geometries on Radar Cross Section

Tai Kim, Ken Vaccaro, Dean Mensa, Don Hilliard

Naval Air Warfare Center Weapons Division, Radar Reflectivity Laboratory, Point Mugu, California 93042, USA
tai.kim@navy.mil
kenneth.vaccaro@navy.mil
dmensa@roadrunner.com
dhilliard@mindspring.com

***Abstract*---This paper examines the effects of bistatic radar geometries on target scattering. Focusing on the signal phase change associated with increasing bistatic angle, the paper examines various effects observed in bistatic versus monostatic RCS.**

1. INTRODUCTION

In contrast to monostatic radar for which the transmitter and receiver are collocated, bistatic radar is characterized by the physical separation between the transmitter and receiver; the angle between the lines-of-sight from the target to the transmitter and the receiver defines the bistatic angle, β. While most radar cross section (RCS) characterization applies to monostatic conditions, bistatic RCS is also of interest because these geometries occur during portions of semi-active missile engagements and because they can enhance radar signatures to improve detection and tracking. In addition to influencing the target RCS, bistatic radar geometries impose predictable reductions in the phase of signals scattered by a target as bistatic angle is increased. These effects influence ISAR (Inverse Synthetic Aperture Radar) imaging.

Interest in bistatic radar, spanning more than 70 years, peaked in the 1950's and 60's during the early development of semi-active radar guided missiles. An excellent technical and historical overview is provided by Jerome Glaser's 1989 IEEE paper [1]. In 1965, Robert Kell formulated the *bistatic—monostatic equivalence theorem*, which showed that, for shallow bistatic angles, the RCS could be estimated from monostatic RCS for angles corresponding to the bistatic bisector angle [2]. Other useful treatments on the topic are contained in [3, pp. 177-183], [4], and [5]. In the course of RCS testing and analysis over the years at the Naval Air Warfare Center Weapons Division, (NAWCWD), Radar Reflectivity Laboratory (RRL) at Point Mugu, California, unique differences have been observed between bistatic and monostatic RCS that become increasingly notable for large values of β.

Examples of monostatic and bistatic RCS testing are shown in the photos of Figures 1 and 2, taken in the largest of the three anechoic chamber test facilities. The arrows shown in Figure 1 represent the transmitted and received signal paths that propagate from the feed antenna, reflected by the compact range collimator to irradiate the target; the signal propagated along the reverse path and captured by the receiver constitutes the monostatic scattering. For the bistatic RCS test shown in Figure 2, the compact range collimator is not used; instead a transmitting antenna is mounted on the lower tower shown at the lower left of the photo and a receiving antenna is mounted atop the large tower shown at upper right of the photo. The bistatic angle, β, is shown between the arrows. The target is rotated in azimuth angle in both monostatic and bistatic tests while the frequency is swept over a wide band of frequencies for each of fine angular increments.

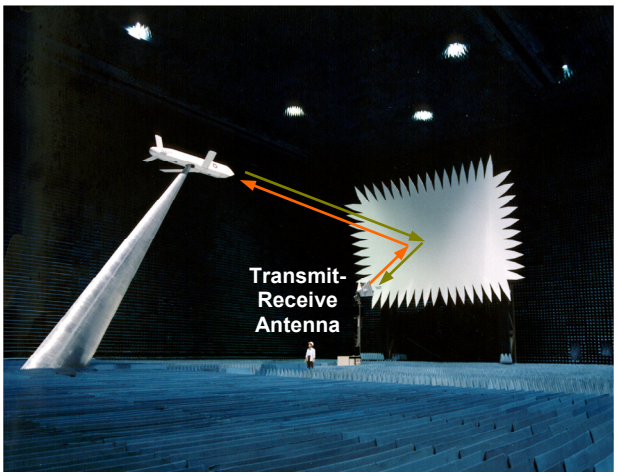

Figure 1. Monostatic RCS Testing.

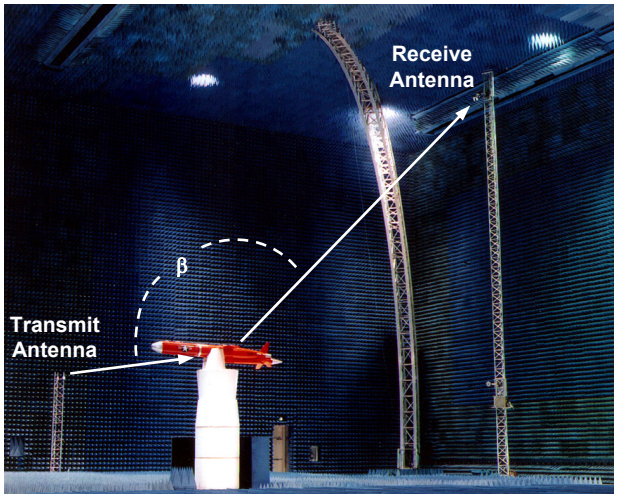

Figure 2. Bistatic RCS Testing.

NAVAIR Public Release 10-1106- Approved for public release; distribution is unlimited

II. EFFECTS OF BISTATIC GEOMETRY

Bistatic effects on RCS are twofold: 1) the RCS magnitude dependence and 2) the phase of the scattered signal response. The first factor is governed by electromagnetic scattering considerations. A field incident on the object induces currents resulting in scattered fields; the incident and scattered fields are constrained by boundary conditions that establish them. The magnitude of the scattered field observed at a far distance from the object defines the RCS. Because the scattered field depends on the object geometry and spectral response, RCS varies as a function of viewing angle and frequency. Although the physical processes that determine RCS of an object are identical for both geometries, monostatic and bistatic RCS differ owing to the different incident and scattered field directions relative to the object. Propagating electromagnetic signals are characterized by the phasor $S = Ae^{j\varphi}$ where A and φ are the signal magnitude and phase, respectively. We are interested in the dependence of S, A, and φ on bistatic angle. The RCS of extended scatterers varies with bistatic angle as pointed out in Ruck, et.al [6]. Because scattering responses of extended objects are determined by the induced current distribution, approaches for determining monostatic and bistatic scattering magnitudes involve analytic estimations, computational solutions to Maxwell's equations, or empirical measurements.

While RCS is determined by the magnitude of the scattered field, many scattering properties of interest are influenced by the phase of the scattered response. These include amplitude scintillation, angular glint, and ISAR images. The following section addresses the effects of bistatic geometries on the phase of scattered signals relative to monostatic conditions. The total phase comprises temporal and spatial components. Because the temporal phase, expressed by $2\pi ft$, where f is the measured temporal frequency and t is time, does not change with bistatic angle, the following treatment concerns the spatial phase dependence on bistatic angle. The round-trip distance from transmitter to receiver determines the received spatial phase.

Figure 3 illustrates a unit-amplitude point scatterer observed by a monostatic radar. The point is located at polar coordinates L,θ relative to the line of sight and the center of rotation, which establish the phase reference for the radar located in the far field. For the monostatic case, the received signal phase is: exp(-j2kr) where k is the wave number $2\pi/\lambda$ and the distance $r = L\cos(\theta)$ is the projection of the scattering point onto the radar line of sight. The sinusoidal function indicates the number of phase cycles incurred by the distance L to the scatterer.

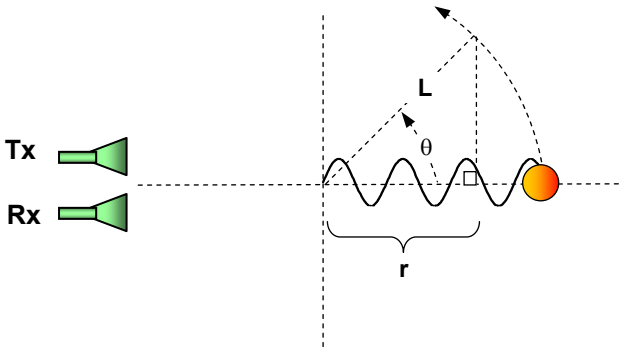

Figure 3. Relative Spatial Phase of a Single Revolving Scatterer in the Presence of Monostatic Radar.

Figure 4 illustrates the identical point scatterer observed by a bistatic radar. The most convenient representation uses a reference centered on the bistatic bisector angle, represented by the horizontal line in Figure 4. As the bistatic angle increases, the distances along the lines of sight are foreshortened. From the geometry of Figure 4, it is clear that both r_1 and r_2 are foreshortened by the cosine of β/2 ; the received signal phase is thus: $\exp[-jk(r_1+r_2)] = \exp[-j2kr\cos(\beta/2)]$.

If the term cos(β/2) is absorbed by the k term, the bistatic phase is identical to the monostatic phase associated with a temporal frequency reduced by cos(β/2). This equivalence is the basis for the treatment of [2]. As noted in [2], caution is required when using this equivalence in practice because the bistatic equivalence is based on the spatial phase reduction caused by the reduced path length and does not account for the intrinsic spectral RCS response of the scattering features associated with the measured temporal frequency.

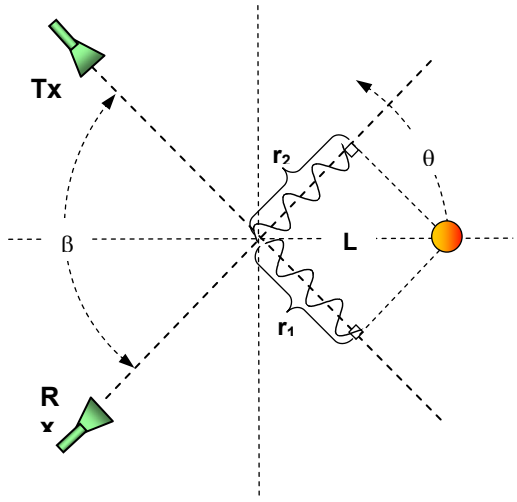

Figure 4. Relative Spatial Phase of a Single Revolving Scatterer in the Presence of Bistatic Radar.

Phase variations for various bistatic angles, shown in Figure 5, illustrate the signal phase reduction with increasing bistatic angle. The transmitters and receivers are shown in the upper and lower quadrants, respectively. The waveforms shown to the left of each receiver consist of the real part of the bistatic responses as a function of target rotation. As the bistatic angle increases, the cyclic variations become less rapid, reducing to zero for β=180°.

The spatial phase is the source of information for mapping target scatter locations onto a geometric grid such as in ISAR imaging. Spatial resolution is proportional to the phase cycle density on the spatial grid, which, as shown above, is maximized for monostatic conditions. Another way to view this is by noting that since a radar can only detect the phase of the total signal path, r_1+r_2, the measurable spatial phase depends on transmit and receive axes' relative orientation. Although the actual spatial size of the phase cycle is the same, the observable number of phase cycles over a given projection is reduced with bistatic angle as presented above, which can be viewed as a closing aperture in the spatial spectrum. In addition, increasing bistatic angle orients the scattered fields in the direction of the transmitted field, which increases the phase coherence of all scatterers within the radar field of view.

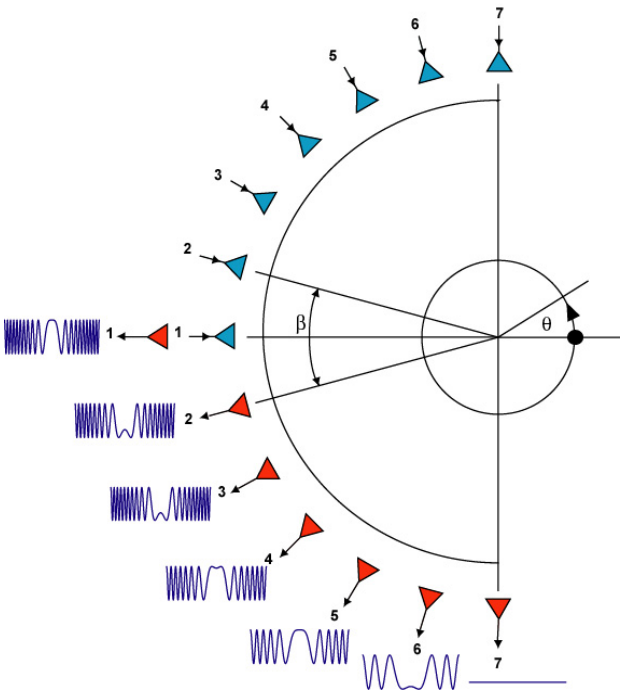

Figure 5. Phase Variations with Increasing Bistatic Angle.

Amplitude Scintillation

The term refers to fluctuations in the RCS of complex targets caused by interference between signals from multiple scattering sources in the radar field of view that form the composite RCS. The phase of individual scatterers depends on 2kr, where k normalizes the signal propagation path length into the number of phase cycles in radians. As the target is viewed for differing angles or frequencies, interference between signals from multiple scattering sources cause the total RCS to fluctuate at a rate determined by the rate of change of phase with angle or frequency. Radars viewing a target in motion at a fixed frequency will receive temporally fluctuating RCS known as amplitude scintillation [7]. Because a bistatic geometry effectively reduces k by cos(β/2), the scintillation rate is reduced accordingly. A reduction in the effective wavenumber also causes a reduction in the rate of RCS fluctuation with frequency. Figure 6 shows amplitude scintillation for two scatterers separated by 5 wavelengths with amplitude 1 and 0.8 for monostatic (left) and 120° bistatic (right) conditions. The amplitude scintillation rate is reduced for the bistatic geometry.

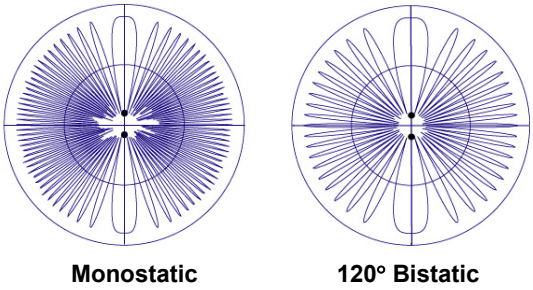

Figure 6. Amplitude Scintillation for Dual Point Target for Monostatic and 120° Bistatic Conditions.

Angular Glint

The term refers to variations in the apparent angle of arrival of the target echo. Because all radars sense the angular location of the target to be in a direction normal to the wavefronts of the received signal, angular glint causes boresight errors that are especially harmful to guided missile seekers. Signals scattered by a point target consist of spherically-expanding wavefronts: the normal to the wavefronts, therefore, is directed to the target point [7]. As the viewing angle for a complex target varies, interference among the various scatterers distorts the wavefronts causing a pointing error. As in the case for amplitude scintillation, bistatic geometries reduce the effective wavenumber thus causing less rapid fluctuations in the total phase and thus less rapid angular errors. Figure 7 shows an example of wavefront distortion resulting from monostatic (left) and 120° (right) bistatic conditions for the dual target of the preceding example. As the viewing angle varies, the observed wavefront disturbances distortion occurs at a slower rate.

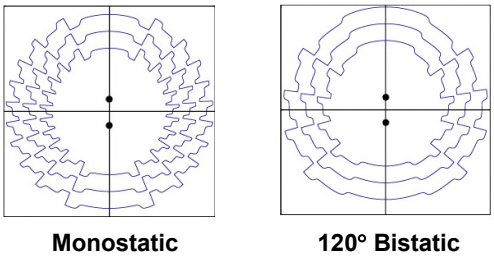

Figure 7. Wavefront Distortion of Dual Point Target for Monostatic and 120° Bistatic Conditions.

ISAR Imaging

Effects of bistatic geometries on ISAR imaging are conveniently analyzed using a k-space viewpoint, summarized in the appendix, which shows that the spatial image is the Fourier transform of the k-space region accessed by the measured data. Figure 8 is a representation of the k space obtained from measurements over a range of frequency and angle, plotted on radial and angular coordinates, respectively and indicated by the shaded regions.

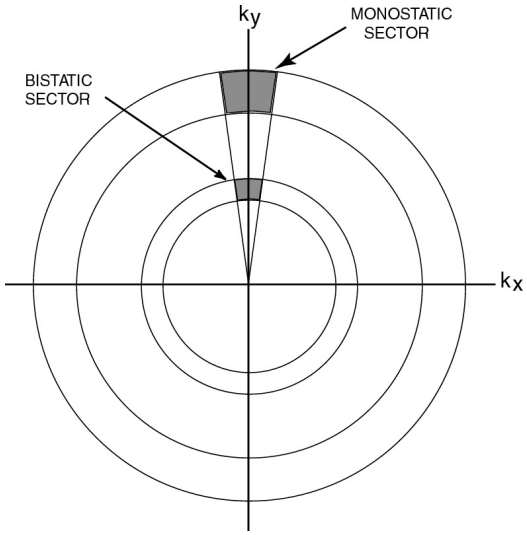

Figure 8. k-space Regions Accessed by ISAR Measurements.

Processing the data from the shaded region of the outer annulus, obtained by monostatic measurements, results in a two-dimensional image with individual scattering points in their proper location and spatial resolution inversely proportional to the extent of the shaded region. The inner annulus corresponds to data from measurements with a bistatic angle of 120°. Because $\cos(\beta/2) = 0.5$, these data are equivalent to monostatic data obtained with half the frequency. The image process associates the bistatic data with values of k reduced by the $\cos(\beta/2)$ factor; that is, the imaging algorithm uses a set of reduced k therefore rendering the image with scatterers in their proper spatial location but with a reduction in spatial resolution by the factor $\cos(\beta/2)$. If the bistatic data are (incorrectly) processed using the unreduced k factors corresponding to monostatic imaging, the resulting image is collapsed radially by the factor $\cos(\beta/2)$. The spatial resolution appears the same as for monostatic since it is computed using the measured temporal bandwidth; however, this constitutes the same loss of resolution because the spatial grid is rescaled to a smaller size by the bistatic geometry.

The algorithm summarized in the appendix formulates the image in terms of a continuous Fourier transform. Because imaging is normally performed on discrete samples using discrete FFTs, we note that the effective angular sampling increments resulting from bistatic measurements are identical to those for monostatic measurements; however, the effective frequency sampling increments are reduced by a $\cos(\beta/2)$ factor. As shown in [3], the unambiguous range and cross-range image extents are, respectively:

$$R_u = c/2\Delta f \qquad \text{and} \qquad X_u = c/2f\Delta\theta$$

where Δf and $\Delta\theta$ are the frequency and angle increments, respectively. For bistatic cases, $\Delta\theta$ remains the same as for monostatic cases, while f and Δf are reduced by $\cos(\beta/2)$. This means that the range and cross-range extents of the bistatic image are expanded by $1/\cos(\beta/2)$. For a given number of frequency and angle samples, therefore, the resolution and granularity are rendered coarser. We note in passing that data collected under bistatic conditions are oversampled relative to those for monostatic conditions. The collection of bistatic data, therefore, allows some degree of economy in the sampling strategy.

From the above, the bistatic spatial phase collapse presents an apparent increase in scatterer coherence. Whatever the bistatic amplitude effects may be on individual scatterers, increasing bistatic angle tends to electrically unify the spatial phase of all scatterers in the radar field of view. In the limit of forward scattering, the fully collapsed spatial phase results in complete coherence of all observable scatterers. Because there are no detectable phase cycles for forward scattering conditions, all spatial information about the target is lost.

III. MEASUREMENTS

The following shows examples of the above effects. The first example is monostatic and bistatic RCS measurements of a 4" diameter x 6" high right circular cylinder in the RRL Small Anechoic Chamber (SAC). The second is monostatic and bistatic RCS measurements of a 15' long, 8" diameter hemisphere-capped cylinder measured at the Echeron Valley Range (previously known as Junction Ranch), located at NAWCWD, China Lake, CA.

The measurements in the SAC chamber, shown in the photos of Figure 9, were calibrated with a 20"-diameter sphere. The cylinder shown set upright on the edge of the Styrofoam column. Measurements were conducted at bistatic angles of: 0°, 90°, 120°, and 140° at a center frequency of 10 GHz over a 3 GHz bandwidth.

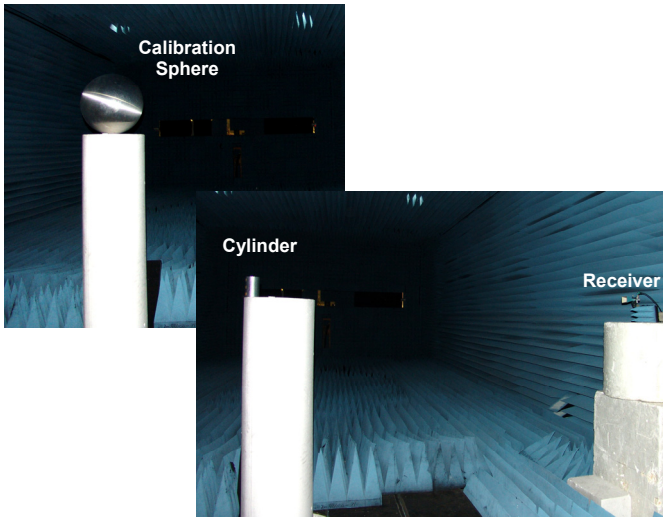

Figure 9. Indoor RCS Measurements in the RRL Small Anechoic Chamber, NAWCWD Point Mugu, CA.

The downrange profile plots of Figure 10 for monostatic and 120° bistatic, show the reduction of bistatic spatial resolution along the downrange axis.

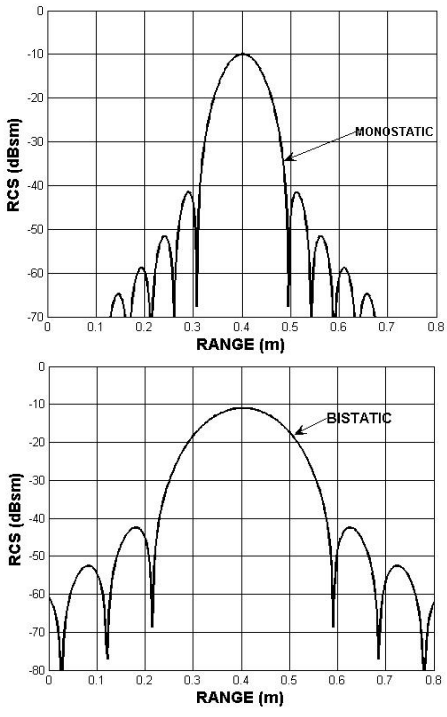

Figure 10. Downrange Profile Comparing the Apparent Cylinder Location From Center of Rotation for Monostatic and 120° Bistatic Conditions.

The ISAR images of Figure 11 for monostatic and 140° bistatic, clearly show the reduction of bistatic spatial resolution resulting from the decreased spatial bandwidth.

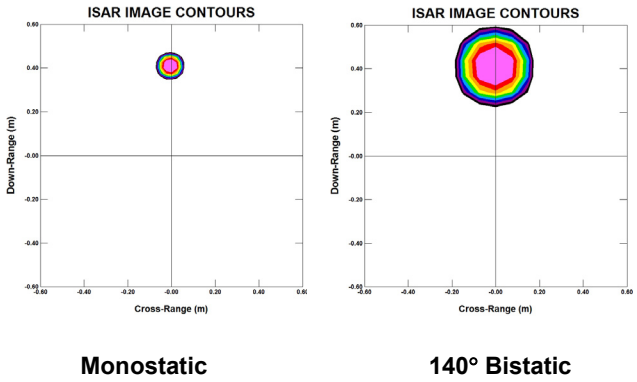

Figure 11. ISAR Image for Monostatic and 140° Bistatic Conditions.

The RCS measurements of the 15' cylinder at the outdoor ground bounce Echeron Valley Range, shown in Figure 12, comprised monstatic and a series of bistatic conditions over a frequency range of 0.2 to 2.0 GHz [8]. The Global RCS plots of Figures 13 and 14 show the monostatic and 145° bistatic frequency and aspect angle signature characteristics, respectively. In these plots, frequency is shown radially and aspect angle is shown on the polar grid. The bistatic result shows a significant change from monostatic with notable reduction in scintillation and a broadening of signature throughout the frequency-angle space as scatterers become increasingly coherent with bistatic angle.

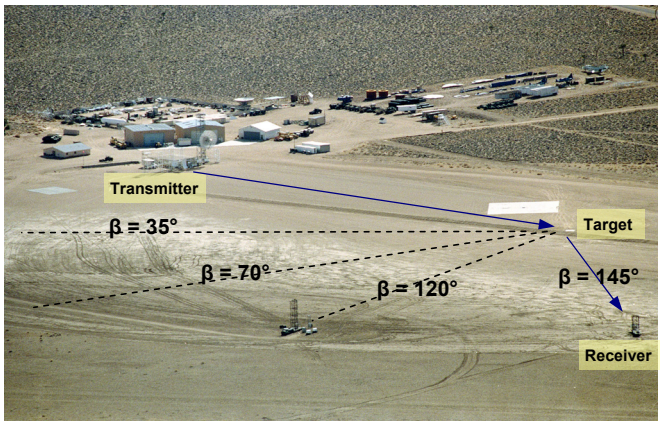

Figure 12. Outdoor RCS Measurements at the Echeron Valley Range, NAWCWD China Lake, CA.

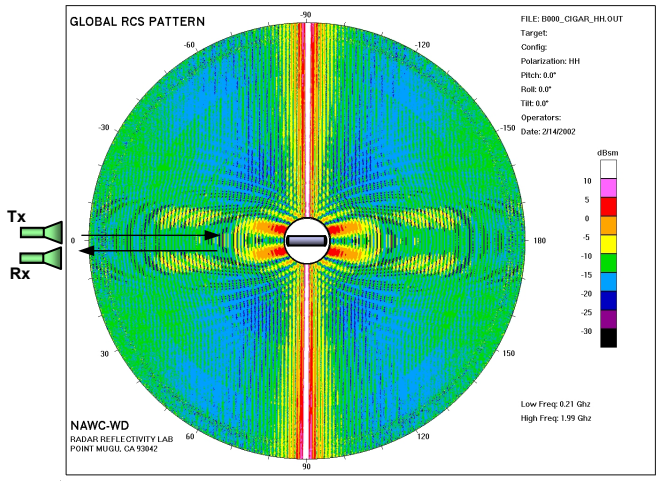

Figure 13. Monostatic Global RCS of 15' Hemisphere-Capped Cylinder.

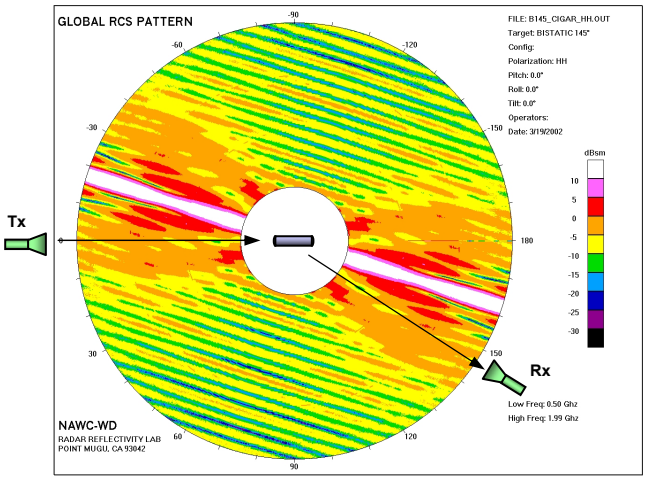

Figure 14. 145° Bistatic Global RCS of 15' Hemisphere-Capped Cylinder.

IV. CONCLUSIONS

In summary, bistatic RCS effects arise in both amplitude scattering mechanisms associated with field-induced currents on the target's scattering surfaces and the reduction of signal phase associated with the bistatic radar geometry. While amplitude effects are highly target dependent, the phase reduction affects the entire scattering volume in the radar field of view.

The k-space representation provides a useful visualization of the bistatic reduction on spatial frequency with the additional benefit of direct correlation to ISAR image space. If the bistatic RCS data are processed using conventional monostatic ISAR imaging, the resulting image is collapsed radially by the factor cos(β/2). The spatial resolution of the incorrectly positioned scatterers appears the same as for monostatic images because it is computed using the measured temporal bandwidth; however, this constitutes the same

loss of resolution because the spatial grid is rescaled to a smaller size by the bistatic geometry.

The bistatic phase reduction causes the total scattered field to appear increasingly coherent compared to monostatic conditions, particularly at and near the forward scattering angle. In the limit of forward scattering, the fully collapsed spatial phase results in complete coherence of all observable scatterers. Because there are no detectable phase cycles for forward scattering conditions, all spatial information about the target is lost.

Finally, as noted in [2], caution should be used when applying the bistatic-monostatic equivalence theorem. The bistatic equivalence is based on the phase reduction caused by the reduced path length and does not account for the intrinsic spectral RCS response of the scattering features associated with the measured temporal frequency.

REFERENCES

[1] J. I. Glaser, *Some Results in the Bistatic Radar Cross Section (RCS) of Complex Objects*, Invited Paper, Proceedings of the IEEE, Volume 77, Issue: 5, pp. 639-648, May 1989

[2] R. E. Kell, *On the Derivation of Bistatic RCS from Monostatic Measurements*, Proceedings of the IEEE, Volume 53, Issue: 8, pp. 983-988, August 1965

[3] D. L. Mensa, *High Resolution Radar Cross-Section Imaging*, Artech House Inc., Boston, London, 1991

[4] D. L. Mensa, G. R. Heidbreder, *Bistatic Synthetic-Aperture Radar Imaging of Rotating Objects*, IEEE Transactions on Aerospace and Electronic Systems, Vol. AES-18, No. 4, July 1982

[5] R. J. Burkholder, I. J. Gupta, J. T. Johnson, *Comparison of Monostatic and Bistatic Radar Images*, IEEE Antennas and Propagation Magazine, Vol. 45, No. 3, June 2003

[6] G. T. Ruck, D. E. Barrick, W. D. Stuart, C. K. Krichbaum, *Radar Cross Section Handbook*, Plenum Press, New York, 1970

[7] D. L. Mensa, *Scintillation Characteristics of Aircraft Targets*, Technical Publication, Naval Missile Center, Point Mugu, CA TP-71-13, CA, March 1971

[8] P. Liesman, W. Schardt, R. Young, *Outdoor Low Frequency Bistatic Far Field Radar Cross Section Meaurements*, Proceedings of the 24th Annual Symposium of the Antenna Measurements and Techniques Association, November 2002

APPENDIX : BISTATIC IMAGING

Figure 1A shows a unit-amplitude point scatterer located at x,y measured by monostatic and bistatic systems at a far-field distance R_0.

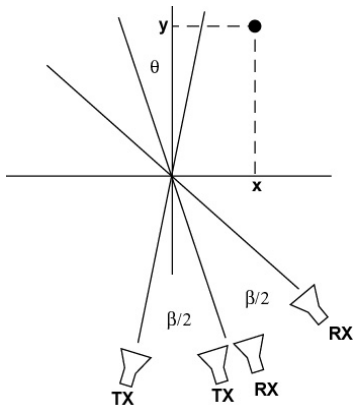

Figure 1A. Monostatic and Bistatic Geometry

The monostatic response observed as a function of the angle θ for a single scatterer is:

$$G_m(k,\theta) = \exp(-j2kR_0)\exp\{j2k[x\sin(\theta) - y\cos(\theta)]\} \quad (1$$

The observed response for a collection of point scatterers g(x,y) is:

$$G_m(k,\theta) = \exp(-j2kR_0)\iint g(x,y)\exp\{j2k[x\sin(\theta) - y\cos(\theta)]\}\,dx\,dy \quad (2$$

If k is considered a vector with components $k_x = k\sin(\theta)$ and $k_y = k\cos(\theta)$, the preceding equation can be expressed as:

$$G_m(k_x,k_y) = \iint g(x,y)\exp\{j2[k_x x - k_y y]\}\,dx\,dy \quad (3$$

where the leading constant term has been omitted for brevity.

Expression (3 constitutes a two-dimensional Fourier transform pair between g(x,y) and $G(k_x,k_y)$. Exploiting this relation, the image can be expressed as an inverse Fourier transform by:

$$g(x,y) = \iint G_m(k_x,k_y)\exp\{-j2[k_x x - k_y y]\}\,dk_x,dk_y \quad (4$$

By a similar development, the bistatic response for a single scatterer is:

$$G_b(k,\theta) = \exp(-j2kR_0)\exp\{j2k[\cos(\beta/2)][x\sin(\theta) - y\cos(\theta)]\} \quad (5$$

The observed response for a collection of point scatterers is:

$$G_b(k,\theta) = \exp(-j2kR_0)\iint g(x,y)\exp\{j2k[\cos(\beta/2)][x\sin(\theta) - y\cos(\theta)]\}\,dx\,dy \quad (6$$

By again considering k to be a vector with components $k_x = k\sin(\theta)$ and $k_y = k\cos(\theta)$, (6 can be expressed as:

$$G_b(k_x,k_y) = \iint g(x,y)\exp\{j2[\cos(\beta/2)][k_x x - k_y y]\}\,dx\,dy \quad (7$$

Then:

$$g(x,y) = \iint G_b(k_x,k_y)\exp\{-j2[\cos(\beta/2)][k_x x - k_y y]\}\,dk_x\,dk_y \quad (8$$

As indicated by (4 , the monostatic image is obtained by a Fourier transform of the measured data; the bistatic image expressed by (8 is obtained by a Fourier transform of the measured data with the k factors reduced by the factor cos(β/2). Figure 2A shows the regions of k space accessed by the monostatic and 120° bistatic data, shown by the outer and inner shaded sectors, respectively.

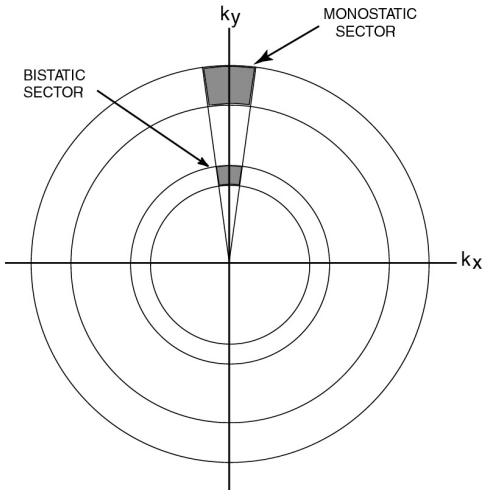

Figure 2A. Regions of k-space Accessed by Monostatic and 120° Bistatic Data.